Flexible and High-Performance Electrochromic Devices Enabled by Self-Assembled 2D TiO2/MXene Heterostructures

Ran Li
Donghua University, Boston University
Xiaoyuan Ma
Boston University
Jianmin Li
Donghua University
Jun Cao
Boston University
Hongze Gao
Boston University
Tianshu Li
Boston University
Xiaoyu Zhang
Donghua University
Lichao Wang
Donghua University
Qinghong Zhang
Donghua University https://orcid.org/0000-0002-4373-7665
Gang Wang
Donghua University
Chengyi Hou
Donghua University
Yaogang Li
Donghua University
Tomas Palacios
Massachusetts Institute of Technology
Yuxuan Lin
UC Berkeley https://orcid.org/0000-0003-0638-2620
Hongzhi Wang
State Key Laboratory for Modification of Chemical Fibers and Polymer Materials, College of Materials Science and Engineering, Donghua University, Shanghai 201620

Xi Ling (xiling@bu.edu)
Boston University

Article

Keywords: Transition metal oxides, TMO, MXenes, EC devices, large-area flexible devices

Posted Date: July 28th, 2020

DOI: https://doi.org/10.21203/rs.3.rs-45725/v1

Version of Record: A version of this preprint was published at Nature Communications on March 11th, 2021. See the published version at https://doi.org/10.1038/s41467-021-21852-7.

Flexible and High-Performance Electrochromic Devices Enabled by Self-Assembled 2D TiO_2/MXene Heterostructures

Ran Li[1,2]†, Xiaoyuan Ma[2]†, Jianmin Li[1], Jun Cao[2], Hongze Gao[4], Tianshu Li[4], Xiaoyu Zhang[1], Lichao Wang[1], Qinghong Zhang[1], Gang Wang[1], Chengyi Hou[1], Yaogang Li[1], Tomás Palacios[3], Yuxuan Lin[3*#], Hongzhi Wang[1*], and Xi Ling[2,4,5*]

[1]State Key Laboratory for Modification of Chemical Fibers and Polymer Materials, College of Materials Science and Engineering, Donghua University, Shanghai 201620, China.

[2]Department of Chemistry, Boston University, 590 Commonwealth Avenue, Boston, MA 02215, USA.

[3]Department of Electrical Engineering and Computer Science, Massachusetts Institute of Technology, Cambridge, MA 02139, USA.

[4]Division of Materials Science and Engineering, Boston University, 15 St. Mary's street, Boston, MA 02215, USA.

[5]The Photonics Center, Boston University, 8 St. Mary's street, Boston, MA 02215, USA.

†These authors contributed equally to this work.

[*]Correspondence to: (X.L.) xiling@bu.edu; (H.W.) wanghz@dhu.edu.cn; (Y.L.) yxlin@berkeley.edu

[#]Current address: Department of Electrical Engineering and Computer Sciences, University of California, Berkeley, CA 94720, USA.

Abstract

Transition metal oxides (TMO) are promising electrochromic (EC) materials for applications such as smart windows and displays, yet challenge still exists to achieve good flexibility, high coloration efficiency and fast response simultaneously. MXenes (e.g. $Ti_3C_2T_x$) and their derived TMOs (e.g. 2D TiO_2) are good candidates for high-performance and flexible EC devices because of their 2D nature and the possibility of assembling them into loosely networked structures. Here we demonstrate flexible, fast, and high-coloration-efficiency EC devices based on self-assembled 2D $TiO_2/Ti_3C_2T_x$ heterostructures, with the $Ti_3C_2T_x$ layer as the transparent electrode, and the 2D TiO_2 layer as the EC layer. Benefiting from the well-balanced porosity and connectivity of these assembled nanometer-thick heterostructures, they present fast and efficient ion and electron transport, as well as superior mechanical and electrochemical stability. We further demonstrate large-area flexible devices which could potentially be integrated onto curved and flexible surfaces for future ubiquitous electronics.

Introduction

Electrochromic (EC) materials, which can change their optical absorption reversibly due to the electrochemical redoxation with inserted ions under an applied potential (*1–3*), have shown great promise in applications such as displays, smart windows and optical camouflage (*3–5*). With the growing interest in bringing electrochromism to the field of flexible and wearable electronics in recent years, incorporating the functionality of flexibility to EC devices while maintaining high energy efficiency, fast switching speed and long durability has become increasingly critical (*6*, *7*). However, this is an extremely challenging task because: (a) both the EC performance and the mechanical properties are non-trivially correlated with the materials of choice, their nanoscale formations, and the assembly approach; and (b) the co-optimization of the transparent conductive electrode and the EC material, as well as the way to integrate them is needed.

Recently, two-dimensional (2D) transition metal carbides, nitrides, and carbonitrides (referred to as MXenes) have emerged (*8*, *9*) as promising nanoscale electronic materials with good electrochemical stability. They have also been reported as promising templates for the synthesis of functional micro/nano-structured materials such as transition metal oxides (TMOs), alkali-metal titanates, and their hybrids (*10*, *11*). Owing to their unique optical and electrical properties, MXenes and their derivatives have demonstrated their potential in the application of energy storage, catalysis and electronics (*12–14*). More importantly, 2D nanosheets of both MXenes and their derivatives can be produced in liquid phase scalably, which makes it easy for constructing self-assembled films and hybrid structures, suitable for device applications in large scale.

We propose that self-assembled MXene/TMO heterostructures, with the MXenes as the flexible transparent electrode, and the TMOs (derived from the MXenes) as the flexible EC layer, are ideal for high-performance and flexible EC devices, yet it has never been explored previously. In addition to the advantage of the easiness of fabrication and integration with different functional

components from MXene derivatives as mentioned above, an even more important reason is that the nanosheets network of TMOs, such as tungsten oxide (WO_3) and titanium oxide (TiO_2), can potentially realize not only superior EC properties, but also reliable mechanical and chemical stability among various candidates of EC materials. First, these inorganic materials are long-lasting and robust against environmental factors such as high temperature, ultraviolet radiation, and mechanical wear (*15–17*), as compared to their organic counterparts (*18*). Second, the nanostructured TMO network, especially in the form of 2D nanosheets, improves electrical and ionic transport significantly, because: (a) the increased surface-to-volume ratio of nanosheets as compared to the bulk forms leads to larger interface areas with the electrolyte and the shorter ion diffusivity pathways within the nanostructured channels (*3*, *19*); and (b) the 2D formation of the nanostructures makes the contact area between adjacent nanosheets much bigger than that between 1D or 0D structures (nanowires or quantum dots) (*20*), which promotes the inter-nanosheets electron transfer (*21*). Finally, networks of 2D nanostructures also helps to redistribute the induced strain more evenly, thus improving both the mechanical strength and the flexibility of the film, which is fundamentally more advantageous than 1D or 0D nanostructures (*22*).

As a proof-of-concept demonstration, we sucessfully assemble $Ti_3C_2T_x$ (T = O, OH or F) and the derived TiO_2 nanosheets into uniform nanometer-thick films at a liquid-liquid interface, and fabricate EC devices based on the TiO_2/$Ti_3C_2T_x$ heterostructures on a flexible substrate. Due to the excellent ion and electron conductivity of assembled single-flake-layer TiO_2 film and the 2D nature of both the MXene electrodes and the TiO_2 EC layer, our devices are among the best flexible EC devices with the fastest coloration speed, the highest coloration efficiency and superior electrochemical stability. We further demonstrate a large-area flexible device which could potentially be integrated with arbitrary curved and flexible surfaces for future ubiquitous electronics.

Results

Fabrication of $TiO_2/Ti_3C_2T_x$ heterostructures

Fig. 1 illustrates the fabrication process of the self-assembled $TiO_2/Ti_3C_2T_x$ heterostructure on a flexible structure as the core functional component of EC devices. The fabrication process consists of three steps: First, the $Ti_3C_2T_x$ nanosheet dispersion in deionized (DI) water is obtained from selective etching of Ti_3AlC_2 powder (MAX phase) (*23*), and diluted to 0.2 mg/L, followed by the formation of the $Ti_3C_2T_x$ aerogel through freeze-drying. The $Ti_3C_2T_x$ aerogel is then annealed in air at 400°C to fully convert the $Ti_3C_2T_x$ aerogel to the TiO_2 aerogel. Second, the $Ti_3C_2T_x$ (TiO_2) aerogels are dispersed into isopropyl alcohol (IPA) to form the $Ti_3C_2T_x$ (TiO_2) solutions, which are then injected into the interface between hexane and water, where the nanosheets self-assemble into uniform nanometer-thick films; Last, the self-assembled $Ti_3C_2T_x$ film and TiO_2 film are transferred sequentially onto a flexible polyethylene terephthalate (PET) substrate to form $TiO_2/Ti_3C_2T_x$ heterostructures, in which the $Ti_3C_2T_x$ film serves as the transparent conductive electrode, and the TiO_2 film serves as the EC layer in EC devices.

To obtained anatase phase of TiO_2, which has been demonstrated a good EC materials (*24*), we anneal the $Ti_3C_2T_x$ aerogel in air at 400°C for 50 h. X-ray diffraction (XRD) and Raman spectroscopy of the flakes are measured before and after the thermal annealing process to investigate the compositional and the structural changes. As shown in **Fig. 2A**, after annealing in air at 400°C, new peaks at 26°, 38°, 48°, 54° and 63° appear in the XRD spectra, corresponding to the (101), (112), (200), (105) and (204) planes of anatase phase of TiO_2 (*25*). Raman spectra of $Ti_3C_2T_x$ flakes after annealing confirms the conversion from $Ti_3C_2T_x$ to TiO_2 (**Fig. 2B**), where peaks at 145 cm^{-1} (E_g), 398 cm^{-1} (B_{1g}), 518 cm^{-1} (B_{1g}), and 639 cm^{-1} (E_g) match well with the Raman features of anatase phase of TiO_2 (*26*). X-ray photoelectron spectroscopy (XPS)

characterization further suggests the transformation from $Ti_3C_2T_x$ to TiO_2. It's clearly seen that the peaks for the Ti element in $Ti_3C_2T_x$ (i.e. Ti-C $2p_{3/2}$ (455.3 eV), Ti(II) $2p_{3/2}$ (456.1 eV), Ti(III) $2p_{3/2}$ (457.2)) disappear after the annealing (**Fig. 2C top and Fig. S1**), while peaks at 458.8 eV and 464.8 eV, corresponding to Ti(IV) $2p_{3/2}$ and Ti(IV) $2p_{1/2}$ in TiO_2, become dominant (**Fig. 2C bottom**) (*27*).

To evaluate the morphology and crystallinity of the obtained TiO_2 nanosheets, optical microscopy (OM), transmission electron microscopy (TEM) and atomic force microscopy (AFM) are used to characterize individual flakes of the $Ti_3C_2T_x$ and the converted TiO_2. **Fig. S2** shows the OM images of a typical flake undergoing the annealing treatment at 400°C for 50 h, where the morphology of the flake maintains in the process, the typical flake sizes are around 7 μm. The typical TEM images (**Fig. 2D and 2E**) and the selective area electron diffraction (SAED) patterns (**insets of Fig. 2D and 2E**) indicate that both $Ti_3C_2T_x$ and TiO_2 are in good crystallinity. The AFM images as shown in **Fig. S3** and **Fig. 2F** suggest that the transformation from $Ti_3C_2T_x$ to TiO_2 maintains its 2D nature with smooth surface. The typical thickness of the anatase TiO_2 flakes is about 2 nm (**Fig. 2F**), which is similar to that of $Ti_3C_2T_x$ flakes **(Fig. S3)**. Although the crystal lattice is transformed drastically from hexagonal ($Ti_3C_2T_x$) to tetragonal (anatase TiO_2), our results clearly demonstrate the successful production of $Ti_3C_2T_x$ flakes and their derived TiO_2 flakes, both of which are high quality crystals with nanometer-scale thicknesses and micrometer-scale sizes. In contrast, the crystal structures collapse and re-organize into amorphous or nanoparticles of TiO_2 during the oxidation treatment in previous reports (*10*). We believe that our result is due to the confined reaction on the initial 2D $Ti_3C_2T_x$ flakes, and their good separation from each other in the skeleton of aerogels during the conversion process helps remain the reaction on each 2D

$Ti_3C_2T_x$ flake, which is consistent with our previous results about the conversion from MoS_2 flakes to ultrathin Mo_5N_6 flakes on SiO_2/Si substrates with maintained crystallinity (*28*).

Self-assembled ultrathin MXene films as high-performance transparent electrodes

To obtain large-area homogeneous thin films of the TiO_2 or $Ti_3C_2T_x$ network, a liquid/liquid interfacial self-assembly (LLIA) technique is used (*29*). Specifically, the 2D flakes/IPA dispersion is injected to the interface between hexane and water. Because of the fast dissolution of IPA into the hexane layer, a surface tension gradient is established along the interface (Marangoni force) (*30*). Driving by this Marangoni force, the 2D flakes spreads out quickly and settles at the edge of the liquid interface, that is, either the sidewall of the container or the edge of an already assembled film. By optimizing the amount of the injected 2D flakes/IPA solution, a full coverage is achieved and a continuous 2D thin film is obtained. As shown in the OM image of **Fig. 3A**, the LLIA $Ti_3C_2T_x$ film is homogeneous over a large area. According to the AFM image (**Fig. 3B and Fig. S4**) taken at the selected area in **Fig. 3A**, the $Ti_3C_2T_x$ flakes are all horizontally oriented, and placed next to each other with very small overlaps. This is very different from the films produced by the spray coating or spin coating methods where the orientations of the flakes are randomly distributed, and they are mostly overlapped and bundled (*31*, *32*). To quantify the uniformity of the LLIA film in large area, we extract the height profiles (**Fig. S4**) from the AFM image, use it to calibrate the contrast of the OM image, and obtain the height mapping from the OM image (**Fig. S5**). The height distributions are extracted from both the AFM image (small area) and the OM image (large area) as shown in **Fig. 3C**. It is observed that both distributions peak at around 2 nm, which corresponds to the thickness of 1-layer of $Ti_3C_2T_x$ flakes. The second most significant peak is at around 3.8 nm, which corresponds to the overlapped area of two adjacent flakes (2 layers). These 1-layer and 2-

layer regions are the key functional components for the electrical conductance, which covers 64% and 18% of the film, respectively.

Because of the uniform height distributions and the high 1-layer and 2-layer coverage, the LLIA $Ti_3C_2T_x$ films show both high optical transparency and high electrical conductance, making them ideal for the transparent electrodes of EC devices. The optical and electronic properties are evaluated by ultraviolet-visible (UV-vis) spectrophotometry and a four-point probe resistance measurement technique. The UV-vis spectra of these films with different $Ti_3C_2T_x$ concentrations (amount of injected $Ti_3C_2T_x$ over the total area of the liquid-liquid interface) are presented in **Fig. 3D**. The transmittance of LLIA $Ti_3C_2T_x$ at 550 nm reaches 96.8% when the concentration is 1 μg cm^{-2}, and decreases steadily to 64.3% as the concentration increases to 60 μg cm^{-2} (*33*). The transmittance at 550 nm versus the sheet resistance (R_s) of the LLIA films, together with the data from previously reported techniques, are plotted in **Fig. 3E**. The R_s value of the LLIA $Ti_3C_2T_x$ film reaches 1623 Ω sq^{-1} at a transmittance of 96.9%, 210 Ω sq^{-1} at 94.1%, and 123 Ω sq^{-1} at 87.8%. Comparing the resistances of materials with the similar transparency, our values are lower than MXene films made by other methods like spin coating (201 Ω sq^{-1} at 87%), dip coating (4300 Ω sq^{-1} at 94%), and spray coating (7974 Ω sq^{-1} at 82%), and also lower than other transparent conductive materials such as graphene, and reduced graphene oxide (see **Table S1** for a summary of different transparent conductive materials) (*31*, *32*, *34–41*). Finally, **Fig. 3F** shows that the LLIA $Ti_3C_2T_x$ film can be transferred onto a flexible substrate (e.g. PET) uniformly in large area (~25 cm^2) with very good optical transparency, suitable for transparent conductive films for the proposed EC device structure.

Fast and high efficiency electrochromism in MXene/TiO_2 heterostructures

The flexible $TiO_2/Ti_3C_2T_x$ heterostructure electrodes are fabricated by transferring LLIA TiO_2 films on the $Ti_3C_2T_x$/PET substrates. Because of the well-controlled LLIA process, it is possible to regulate the EC properties simply by the thickness of the TiO_2 layer. As shown in **Fig. 4A,** 1 to 5 layers of the LLIA TiO_2 film are transferred sequentially onto a PET substrate in a layer-by-layer fashion. They are almost indistinguishable at the bleach state, when no bias is applied, but become translucent with different opacity at the colored state, when emerged in an electrolyte solution (1M $LiClO_4$/propylene carbonate (PC)) and biased with a constant negative voltage (-1.6 V). This optical opacity induced by a negative potential is associated with the reduction of TiO_2 by counterions Li^+ and the formation of Li_xTiO_2 (*42*).

The EC performance of the nm LLIA $TiO_2/Ti_3C_2T_x$ heterostructures is much better than previous reports according to the *in-situ* UV-Vis-NIR spectrophotometry. The measured spectra of the $TiO_2/Ti_3C_2T_x$ heterostructures at 0V and -1.6 V biases are shown in **Fig. 4B** and **Fig. S6**, The optical modulation range ΔT is defined as $\Delta T = T_b - T_c = \exp(-\alpha_b L) - \exp(-\alpha_c L)$, where T_b and T_c are the transmittance of the bleach state and the colored state, α_b and α_c represent absorption coefficient of the bleach and the colored state of the LLIA film, and L is the thickness of the film. ΔT at the wavelength of 550 nm increases gradually with the layer numbers of the transferred LLIA TiO_2 films (7.19%, 12.26%, 21.12%, 25.60%, 32.12%, 38.20%, and 41.09% from 1 to 7 layers) **(Table S2)**. The absorption coefficient change $\Delta\alpha$ can be obtained by $\Delta\alpha = \alpha_c - \alpha_b \approx [\ln(T_c/T_b)]/L$, which is a physical parameter independent of geometries of the film, thus can be used to compare different technologies. $\Delta\alpha$ of the LLIA TiO_2 film is extracted to be 0.12 nm^{-1}, which is almost one order of magnitude higher than the previously reported TiO_2-based EC

materials assembled by other methods (**Table S4**) (*20*, *43–54*), suggesting a very high utilization of TiO_2 in the LLIA films during the EC process.

To quantify the utilization rates of both the EC material and the pumped charge, the optical density change ($\Delta OD = \log_{10}(T_b/T)$) as the function of the pumped charge density (Q, calculated by an integration of the driving current density over time) during the coloration half-cycle is measured and plotted in **Figure 4C**. The coloration efficiencies (CE) (*55*), defined as the slope of the ΔOD-Q plot when Q is close to 0, for the LLIA TiO_2 films with 1 to 7 layer numbers are extracted to be 277, 271, 260, 263, 259, 245 and 243 $cm^2\ C^{-1}$, respectively **(Fig. 4C and Table S2)**. These high CE values indicate that small amounts of charge insertion/extraction can result in a large optical modulation, which is a results of high utilization rates of both the EC materials and the pumped charges. High *CE* also guarantees the long-term electrochemical stability. As expected, the LLIA films shows maintained optical contrast (up to 95% of its original value) after 500 EC cycles (**Fig. S7 and S8**). This high cycling stability is essential for practical applications of the EC devices.

The coloration/bleaching time τ_c/τ_b, another important figure-of-merit for EC materials, defined as the time needed for 90% of the total optical change, is also investigated on the LLIA $TiO_2/Ti_3C_2T_x$ heterostructures. The temporal responses of the transmittance at 550 nm are measured as the bias is switched between -1.6 V and 0 V periodically (**Fig. 4D)**. The coloration/bleaching times for 1 to 7 layers of the LLIC TiO_2 films are extracted to be 0.71/0.12 s, 0.73/0.12 s, 1.03/0.20 s, 1.11/0.24 s, 1.08/0.26 s, 1.23/0.29 s and 1.63/0.38 s (also summarized in **Table S2**), which are much shorter than those of reported TiO_2 EC electrode (generally > 10 s) and most reported inorganic materials, and comparable to those of organic EC materials (**Table S4**).

Ion diffusion process inside the EC material plays a crucial role in the EC performance. To further explore the Li^+ diffusion behavior of the LLIA TiO_2 films during the EC process, cyclic voltammetry (CV) and electrochemical impedance spectroscopy (EIS) are measured (details are listed in method section). All LLIA films exhibit one pair of redox peaks in their CV curves, corresponding to the reduction and oxidation of TiO_2 **(Fig. S9)**. According to the EIS results as shown in **Fig. S10** and **Table S3**, the equivalent series resistance (ESR) does not change much as the TiO_2 thickness increases from 1 to 7 layers, and the charge-transfer resistance (R_{ct}) only raises from 8.7 Ω to 15.7 Ω, indicating that multilayer stacking does not decrease the conductivity and charge-transfer speed significantly at the interface of the TiO_2 film and electrolyte.

The apparent ion diffusion coefficient *D*, which represents the kinetics of ion insertion/extraction in the EC film, can be extracted either from the scanning-rate-dependent CV measurements, or from the Warburg region of the Bode plot obtained from the EIS measurements (see methods for details about the extraction methods of *D*) (*56*). As shown in **Fig. 4E**, the *D* values extracted from the CV and from the EIS measurements are 5.05×10^{-14}, 9.63×10^{-14}, 2.68×10^{-13}, 1.15×10^{-12}, 5.45×10^{-12}, 6.29×10^{-12}, and 1.10×10^{-11} $cm^2\ s^{-1}$, and 2.75×10^{-12}, 3.94×10^{-12}, 6.59×10^{-12}, 1.21×10^{-11}, 1.39×10^{-11}, 1.88×10^{-11}, 2.24×10^{-11} $cm^2\ s^{-1}$, respectively, as the number of layer of the TiO_2 film increases from 1 to 7. The positive correlation between *D* and the layer number can be attributed to the increased electrochemical area of the LLIA TiO_2 film due to its high surface-to-volume ratio, which will be explained later.

To benchmark the overall EC performance, the values of *CE* and τ_c of the LLIA $TiO_2/Ti_3C_2T_x$ heterostructures as well as previously reported EC materials are summarized in **Fig. 4F** and **Table S4**. It is clearly observed that both the *CE* and the response time of our proposed structures are several times or even one order of magnitude better than both other materials such

as WO_3, and other nanostructured TiO_2, including dense films and other 0D or 1D nanostructures, and comparable with organic materials. Moreover, LLIA $TiO_2/Ti_3C_2T_x$ heterostructures also show a good cycling stability, addressing the ultraviolet/electrochemical decomposition problem of traditional organic materials in applications (*18*).

We believe that the superiority of the EC performance of the LLIA $TiO_2/Ti_3C_2T_x$ heterostructures mainly results from the 2D nature of the TiO_2 flakes as well as the loosely networked structures. To understand this, we propose two possible ion transport pathways (*19*). The first ion transport pathway is that the Li^+ ions enters the EC material only at the top surface, and the redoxation deeper into the EC material is accessed by inter-crystal-lattice diffusion of Li^+ ions; whereas in the second ion transport pathway (as illustrated in **Fig. 4G**), Li^+ ions could travel to all the surfaces of individual EC nanostructures efficiently in the liquid phase, and as a result, the diffusion and the redoxation take place throughout the entire EC nanostructures simultaneously. For dense films, only the first pathway takes place, resulting in very bad coloration efficiency and very slow coloration/bleaching time; while for nanostructured films (including our 2D nanostructures and previously reported 0D or 1D nanostructures), the second pathway, which is more efficient and much faster, starts to play an important role. The higher probability the second pathway takes place in a nanostructured film, the better EC performance it can achieve.

Our experimental results suggest that the second pathway is the dominating Li^+ ion transport mechanism in the proposed self-assembled 2D TiO_2 films. First, the high *CE* and its small decrease with the thickness suggest that Li^+ ions can easily access all the TiO_2 flakes regardless of the depth of them from the top surface of the film. Second, the color change time τ (τ_c or τ_b) is fast and stays almost the same with different thicknesses. Given that τ is proportional to the square of the depth of the diffusion, we speculate that the effective diffusion depth is likely

to be determined by the average thickness of individual TiO_2 flakes, rather than the thickness of the assembled TiO_2 film. Last, the increasing trend between D and the thickness indicates that it is less likely that the extremely slow inter-nanosheet diffusion is contributed to the measured apparent diffusion coefficient. Instead, D follows a parabolic trend with the thickness (see **Fig. S11**), or the number of layers, which agrees well if considering the contribution from the electrochemical area A_{EC} and assuming a linear increase of A_{EC} with the number of layers, that is, $D \sim (A_{EC}/A)^2 D_0 \propto N^2$, where A is the geometrical area, D_0 is the intrinsic diffusion coefficient, and N is the number of layers. All these experimental observations can be explained well if the performance is governed by the second ion transport pathway, in which all the surfaces of the 2D TiO_2 flakes are interfacing well with the electrolyte, and the actual diffusion length is approximately the thickness of individual TiO_2 flakes (**Fig. 4G**). As a comparison, for 1D or 0D nanostructures, although the ideal surface-to-volume might be even larger, the surfaces may not be fully exposed to the electrolyte because of the denser packing of these nanostructures in a film. Consequently, the Li^+ ions have to undergo the first pathway in order to access the deeper EC materials, which tremendously limits the speed and thus reduces the coloration efficiency.

Flexible MXene/TiO_2 heterostructure EC devices for large-area applications

The overall flexibility of an EC device is determined by the most rigid layer. In our proposed $TiO_2/Ti_3C_2T_x$ heterostructure, both the EC layer and the transparent electrode have superior mechanical bendability. To confirm this, bending test is performed on the as-fabricated LLIA electrode. As shown in **Fig. 5A**, the resistance of the $Ti_3C_2T_x$/PET film increases by only 6% after 1000 bending and release cycles at a bending radius of 0.3 cm, whereas the sheet resistance of a commercial ITO/PET film increases quickly by 3 orders of magnitude after 1000 bending cycles even at a much larger bending radius of 1.5 cm. The EC optical switching behaviors of the

$TiO_2/Ti_3C_2T_x$/PET film and the TiO_2/ITO/PET before and after 1000 bending cycles are also tested (**Fig. 5B**). ΔT of the $TiO_2/Ti_3C_2T_x$/PET electrode remains at 94% of its original value after 1000 bending cycles. In contrast, ΔT of the TiO_2/ITO/PET electrode drops to about 30% after 1000 cycles.

Finally, a large-area flexible EC device with a dimension of 30 cm × 20 cm are demonstrated as an example for practical large-area applications. As shown in **Fig. 5C**, it is composed of a LLIA $TiO_2/Ti_3C_2T_x$ heterostructure on a PET substrate as the EC electrode, another LLIA $Ti_3C_2T_x$/PET film as the counter electrode, and a 1 M $LiClO_4$/PC/Poly(methyl methacrylate) (PMMA) layer as the electrolyte. Benefit from the exceptional optical memory effect of TiO_2 based materials, the EC device can maintain its coloration state after disconnecting from the voltage supply (**Fig. 5D** and **5E**), which is advantageous for energy saving in future applications. The EC device presents a uniform color distribution even in the bending state, which opens up the possibility of scaling up this technology for applications such as flexible displays, smart windows, and other ubiquitous electronics.

Discussion

In summary, high performance and flexible EC devices are realized based on assembled 2D $TiO_2/Ti_3C_2T_x$ heterostructures. This success benefits from several important achievements in this work, including the realization of single crystalline 2D TiO_2 flakes with micrometer-scale sizes and nanometer-scale thicknesses, and the liquid/liquid interfacial self-assembly technique enabled mass production of self-assembled MXene and 2D TMO films with good uniformity. We expect our approach to synthesize 2D TiO_2 crystals to be developed to a general methodology for the synthesis of high-quality 2D MXene derivatives. Also, the self-assembled MXene films could be used as flexible, transparent, and porous electrodes in large-scale electronic, optoelectronic and

energy-harvesting applications. Our performance test clearly shows that exceptional electrochromic efficiency, fast coloration speed, and good flexibility are achieved simultaneously on the self-assembled 2D TMO/MXene heterostructures based EC devices, which is attributed to the unique electrical, electrochemical, and mechanical properties of the networks of 2D nanostructures. Finally, a large-area flexible electrochromic device is demonstrated, paving the way for integrating electrochromic devices to next-generation flexible and wearable electronics.

Materials and Methods

Chemicals

All the starting materials are available commercially and used as received. Polyethylene terephthalate (PET) was rinsed sequentially in the baths of deionized water, acetone, and isopropanol. Ti_3AlC_2 (MAX-Phase, purchased from 11 Technology Co. Ltd), lithium fluoride (LiF, Alfa Aesar, 99.99%), hydrochloric acid (HCl, Fisher Chemical, 6M), 1-hexene (Acros Organics, 99%), isopropyl alcohol (IPA, Fisher Chemical, 99%), propylene carbonate (PC, Alfa Aesar, 99%), lithium perchlorate ($LiClO_4$, Acros Organics, 99+%), poly(methyl methacrylate) (PMMA, ACROS Organics, M.W. 35000) were utilized without initial treatments.

Synthesis and interfacial assembly of $Ti_3C_2T_x$ and 2D TiO_2 films

Ti_3AlC_2 etching was performed following Gogosti's work(*23*) to prepare 2D $Ti_3C_2T_x$. Briefly, 1.6 g lithium fluoride was dissolved into 5 mL of DI water with 15 mL 12 M hydrochloric acid solution in plastic bottle as the etchant solution. Then 1 g Ti_3AlC_2 (MAX phase) powders was gradually added to the etchant solution within 5 minutes and the reaction is maintained with stirring the reactants at 40°C in a silicon oil bath for 24 h. Etched MXene was washed with DI water, and isolated by centrifugation at 3500 rpm for 5 minutes. Washing was repeated several times until a stable dark supernatant solution of $Ti_3C_2T_x$ flakes with a pH value of around 6 was obtained. The solution was subsequently centrifuged for 30 minutes at 3500 rpm, after which a dark sediment of $Ti_3C_2T_x$ was observed and then collected.

To obtaine the TiO_2 aerogel, the $Ti_3C_2T_x$ gel was diluted to 0.2 mg/ml with DI water, then the solution were freeze dried at -47℃ for days to form an aerogel. Next, the $Ti_3C_2T_x$ aerogel was put in a ceramic boat and annealed at the temperature of 400℃ for 50 h with the heating rate of 1℃/min.

To assemble the $Ti_3C_2T_x$ flakes into a continuous film, the $Ti_3C_2T_x$ aerogel was dispersed in an IPA solution (2 mg/ml) by sonicating for 30 minutes. Hexane (with a height of ~2 cm) was carefully poured on the top of DI water (with a height of ~6 cm) to set up an interface between these two liquids. Then, the $Ti_3C_2T_x$/IPA dispersion was slowly injected near the interface to form a continuous film. After removing the top hexane layer, the self-assembly film was transferred onto a substrate and annealed at 90℃ in vacuum for 50 h (<0.05 MPa).

The assembly for the TiO_2 films is similar to the $Ti_3C_2T_x$ assembly process. For multilayered TiO_2, the transferred films were dried at 60 ℃ in vacuum for 1 h, and then treated with oxygen plasma (the oxygen gas flow rate is 50 SCCM, and power is 100 W) for 30 s before each cycle, then the $TiO_2/Ti_3C_2T_x$ heterostructures were annealed at 90℃ in vacuum (<0.05 MPa) for 50 h before use.

Assembly of the Electrochromic device

The electrolyte gel was obtained by mixing 1 M $LiClO_4$ in a PC solution and 20 wt% PMMA (relative to the $LiClO_4$/PC solution). The EC devices were fabricated by hot pressing the electrolyte gel sandwiched by the $TiO_2/Ti_3C_2T_x$/PET electrodes and the $Ti_3C_2T_x$ /PET counter electrode with a scotch tape spacer (with the thickness of 1 mm) at 60℃.

Material characterization

The X-ray diffraction (XRD) patterns were measured using an X-ray diffractometer (Bruker AXS X8 Proteum-R instrument) with the radiation at 40 kV and 200 mA. Raman spectroscopy measurements were performed on a Renishaw inVia Raman microscope equipped with a 532 nm laser line (The laser power on the samples is about 1.6 mW). All the spectra in comparison were taken under the same conditions. Transmission electron microscopy (TEM) measurements were performed on a FEI Tecnai Osiris TEM. Selected area electron diffraction (SAED) was measured

on a JEOL 2100 TEM. The AFM measurements were conducted on a Bruker Dimension system. X-ray photoelectron spectroscopy (XPS) measurements were performed using a PHI Versaprobe II. The UV-vis spectroscopy was carried out using a Agilent CARY 5000.

Electrochemical measurements and parameter extraction

Electrochemical measurements were carried out in a PC solution containing 1 M $LiClO_4$ electrolyte using three-electrode electrochemical cells with the TiO_2/ $Ti_3C_2T_x$/PET films as the working electrodes, a platinum plate as the counter electrode, and a freshly prepared Ag/Ag^+ as the pseudo-reference electrode (calibrated by ferrocene). Electrochemical impedance spectroscopy (EIS) and cycle voltammetry (CV) were conducted by an electrochemical workstation (Bio-logic SAS, VSP-300) over a frequency range of 100 mHz-1000 KHz.

The measured EIS spectra was fitted with a circuit model illustrated in **Fig. S10**. As shown in **Fig. S10**, the Nyquist plot of all films is composed of three parts: an equivalent series resistance (*ESR*) in series with a semicircle consisting of a non-faradaic double layer capacitance (C_{dl}) and a charge-transfer resistance (R_{ct}) at high frequency; a 45° linear region representing the Warburg element (W), which captures the ion diffusion process at medium frequency; and a line related to the capacitive charging behavior of the pseudo-capacitance (C_p) of TiO_2 film and its bulk resistance (R_p) at low frequency.

The apparent ion diffusion coefficient D can be extracted from both the EIS measurements and the CV measurements. In the first method, D_{EIS} can be calculated from the Warburg region according to equations (1) and (2) (*56*, *57*):

$$Z_w = \sigma\omega^{-1/2} \quad (1)$$

$$D_{EIS} = R^2T^2/(2A^2n^4F^4C^2\sigma^2) \quad (2)$$

where σ is the slope of Z_w against $\omega^{-1/2}$, R is the gas constant, T is the absolute temperature, A is the effective working area (geometrical area), n is the number of electrons involved in the electrochemical reaction, F and C are the Faraday constant and the molar concentration of Li^+ ions.

In the second method, the apparent ion diffusion coefficients D_{CV} can be calculated by:(*58*)

$$i_p = 2.687\times10^5\times n^{3/2}\times D_{CV}^{1/2}\times C\times A\times v^{1/2} \quad (3)$$

where v represents the potential sweeping rate, i_p represents the peak current density.

References

1. D. R. Rosseinsky, R. J. Mortimer, Electrochromic Systems and the Prospects for Devices. *Adv. Mater*. **13**, 783–793 (2001).
2. P. R. Somani, S. Radhakrishnan, Electrochromic materials and devices: present and future. *Mater. Chem. Phys*. **77**, 117–133 (2003).
3. S. Cong, Y. Tian, Q. Li, Z. Zhao, F. Geng, Single-Crystalline Tungsten Oxide Quantum Dots for Fast Pseudocapacitor and Electrochromic Applications. *Adv. Mater.* **26**, 4260–4267 (2014).
4. R. J. Mortimer, A. L. Dyer, J. R. Reynolds, Electrochromic organic and polymeric materials for display applications. *Displays*. **27**, 2–18 (2006).
5. S. Zhang, S. Cao, T. Zhang, A. Fisher, J. Y. Lee, Al^{3+} intercalation/de-intercalation-enabled dual-band electrochromic smart windows with a high optical modulation, quick response and long cycle life. *Energy Environ. Sci*. **11**, 2884–2892 (2018).
6. C. Yan, W. Kang, J. Wang, M. Cui, X. Wang, C. Y. Foo, K. J. Chee, P. S. Lee, Stretchable and Wearable Electrochromic Devices. *ACS Nano*. **8**, 316–322 (2014).
7. R. T. Wen, C. G. Granqvist, G. A. Niklasson, Eliminating degradation and uncovering ion-trapping dynamics in electrochromic WO_3 thin films. *Nat. Mater*. **14**, 996–1001 (2015).
8. Z. Fu, N. Wang, D. Legut, C. Si, Q. Zhang, S. Du, T. C. Germann, J. S. Francisco, R. Zhang, Rational Design of Flexible Two-Dimensional MXenes with Multiple Functionalities. *Chem. Rev.* **119**, 11980–12031 (2019).
9. J. Chen, Q. Huang, H. Huang, L. Mao, M. Liu, X. Zhang, Y. Wei, Recent progress and advances in the environmental applications of MXene related materials. *Nanoscale*. **12**, 3574–3592 (2020).
10. A. Shahzad, K. Rasool, M. Nawaz, W. Miran, J. Jang, M. Moztahida, K. A. Mahmoud, D. S. Lee, Heterostructural $TiO_2/Ti_3C_2T_x$ (MXene) for photocatalytic degradation of antiepileptic drug carbamazepine. *Chem. Eng. J*. **349**, 748–755 (2018).
11. Y. Dong, Z. S. Wu, S. Zheng, X. Wang, J. Qin, S. Wang, X. Shi, X. Bao, Ti_3C_2 MXene-Derived Sodium/Potassium Titanate Nanoribbons for High-Performance Sodium/Potassium Ion Batteries with Enhanced Capacities. *ACS Nano*. **11**, 4792–4800 (2017).
12. J. Pang, R. G. Mendes, A. Bachmatiuk, L. Zhao, H. Q. Ta, T. Gemming, H. Liu, Z. Liu, M. H. Rummeli, Applications of 2D MXenes in energy conversion and storage systems. *Chem. Soc. Rev.* **48**, 72–133 (2019).
13. G. Cai, J. H. Ciou, Y. Liu, Y. Jiang, P. S. Lee, Leaf-inspired multiresponsive MXene-based actuator for programmable smart devices. *Sci. Adv.* **5**, eaaw7956 (2019).
14. P. Salles, D. Pinto, K. Hantanasirisakul, K. Maleski, C. E. Shuck, Y. Gogotsi, Electrochromic Effect in Titanium Carbide MXene Thin Films Produced by Dip-Coating. *Adv. Funct. Mater*. **29**, 1809223 (2019).
15. C. Wang, M. Shim, P. Guyot-Sionnest, Electrochromic Nanocrystal Quantum Dots. *Science*. **291**, 2390–2392 (2001).
16. J. Z. Chen, W. Y. Ko, Y. C. Yen, P. H. Chen, K. J. Lin, Hydrothermally Processed TiO_2 Nanowire Electrodes with Antireflective and Electrochromic Properties. *ACS Nano*. **6**, 6633–6639 (2012).
17. Y. C. Nah, A. Ghicov, D. Kim, S. Berger, P. Schmuki, TiO_2-WO_3 Composite Nanotubes by Alloy Anodization: Growth and Enhanced Electrochromic Properties. *J. Am. Chem. Soc.* **130**, 16154–16155 (2008).
18. J. Jensen, M. V. Madsen, F. C. Krebs, Photochemical stability of electrochromic polymers

and devices. *J. Mater. Chem. C*. **1**, 4826–4835 (2013).
19. C. Wang, M. Shim, P. Guyot-Sionnest, Electrochromic Nanocrystal Quantum Dots. *Science*. **291**, 2390–2392 (2001).
20. A. Azam, J. Kim, J. Park, T. G. Novak, A. P. Tiwari, S. H. Song, B. Kim, S. Jeon, Two-Dimensional WO_3 Nanosheets Chemically Converted from Layered WS_2 for High-Performance Electrochromic Devices. *Nano Lett.* **18**, 5646–5651 (2018).
21. K. Li, Q. Zhang, H. Wang, Y. Li, Lightweight, highly bendable and foldable electrochromic films based on all-solution-processed bilayer nanowire networks. *J. Mater. Chem. C*. **4**, 5849–5857 (2016).
22. L. Liang, J. Zhang, Y. Zhou, J. Xie, X. Zhang, M. Guan, B. Pan, Y. Xie, High-performance flexible electrochromic device based on facile semiconductor-to-metal transition realized by $WO_3 \cdot 2H_2O$ ultrathin nanosheets. *Sci. Rep*. **3** (2013).
23. M. Alhabeb, K. Maleski, B. Anasori, P. Lelyukh, L. Clark, S. Sin, Y. Gogotsi, Guidelines for Synthesis and Processing of Two-Dimensional Titanium Carbide ($Ti_3C_2T_x$ MXene). *Chem. Mater.* **29**, 7633–7644 (2017).
24. Z. S. Khalifa, H. Lin, S. Ismat Shah, Structural and electrochromic properties of TiO_2 thin films prepared by metallorganic chemical vapor deposition. *Thin Solid Films*. **518**, 5457–5462 (2010).
25. R. van de Krol, A. Goossens, E. A. Meulenkamp, In Situ X□Ray Diffraction of Lithium Intercalation in Nanostructured and Thin Film Anatase TiO_2. *J. Electrochem. Soc.* **146**, 3150 (1999).
26. O. Khatim, M. Amamra, K. Chhor, A. M. T. Bell, D. Novikov, D. Vrel, A. Kanaev, Amorphous–anatase phase transition in single immobilized TiO_2 nanoparticles. *Chem. Phys. Lett.* **558**, 53–56 (2013).
27. X. T. Gao, Y. Xie, X. D. Zhu, K. N. Sun, X. M. Xie, Y. T. Liu, J. Y. Yu, B. Ding, Ultrathin MXene Nanosheets Decorated with TiO_2 Quantum Dots as an Efficient Sulfur Host toward Fast and Stable Li–S Batteries. *Small*. **14**, 1802443 (2018).
28. J. Cao, T. Li, H. Gao, Y. Lin, X. Wang, H. Wang, T. Palacios, X. Ling, Realization of 2D crystalline metal nitrides via selective atomic substitution. *Sci. Adv.* **6**, eaax8784 (2020).
29. X. Yu, M. S. Prévot, N. Guijarro, K. Sivula, Self-assembled 2D WSe_2 thin films for photoelectrochemical hydrogen production. *Nat. Commun*. **6**, 7596 (2015).
30. C. V. Sternling, L. E. Scriven, Interfacial turbulence: Hydrodynamic instability and the marangoni effect. *AIChE J*. **5**, 514–523 (1959).
31. C. Zhang, B. Anasori, A. Seral□Ascaso, S. H. Park, N. McEvoy, A. Shmeliov, G. S. Duesberg, J. N. Coleman, Y. Gogotsi, V. Nicolosi, Transparent, Flexible, and Conductive 2D Titanium Carbide (MXene) Films with High Volumetric Capacitance. *Adv. Mater.* **29**, 1702678 (2017).
32. K. Hantanasirisakul, M. Q. Zhao, P. Urbankowski, J. Halim, B. Anasori, S. Kota, C. E. Ren, M. W. Barsoum, Y. Gogotsi, Fabrication of $Ti_3C_2T_x$ MXene Transparent Thin Films with Tunable Optoelectronic Properties. *Adv. Electron. Mater.* **2**, 1600050 (2016).
33. X. Li, T. Yang, Y. Yang, J. Zhu, L. Li, F. E. Alam, X. Li, K. Wang, H. Cheng, C. T. Lin, Y. Fang, H. Zhu, Large-Area Ultrathin Graphene Films by Single-Step Marangoni Self-Assembly for Highly Sensitive Strain Sensing Application. *Adv. Funct. Mater.* **26**, 1322–1329 (2016).
34. K. Min, T. H. Han, J. Kim, J. Jung, C. Jung, S. M. Hong, C. M. Koo, A facile route to fabricate stable reduced graphene oxide dispersions in various media and their transparent

conductive thin films. *J. Colloid Interface Sci.* **383**, 36–42 (2012).
35. G. Ying, A. D. Dillon, A. T. Fafarman, M. W. Barsoum, Transparent, conductive solution processed spincast 2D Ti_2CT_x (MXene) films. *Mater. Res. Lett.* **5**, 391–398 (2017).
36. M. Mariano, O. Mashtalir, F. Q. Antonio, W. H. Ryu, B. Deng, F. Xia, Y. Gogotsi, A. D. Taylor, Solution-processed titanium carbide MXene films examined as highly transparent conductors. *Nanoscale*. **8**, 16371–16378 (2016).
37. G.-M. Weng, J. Li, M. Alhabeb, C. Karpovich, H. Wang, J. Lipton, K. Maleski, J. Kong, E. Shaulsky, M. Elimelech, Y. Gogotsi, A. D. Taylor, Layer-by-Layer Assembly of Cross-Functional Semi-transparent MXene-Carbon Nanotubes Composite Films for Next-Generation Electromagnetic Interference Shielding. *Adv. Funct. Mater.* **28**, 1803360 (2018).
38. S. J. Kim, J. Choi, K. Maleski, K. Hantanasirisakul, H. T. Jung, Y. Gogotsi, C. W. Ahn, Interfacial Assembly of Ultrathin, Functional MXene Films. *ACS Appl. Mater. Interfaces*. **11**, 32320–32327 (2019).
39. C. Zhang, V. Nicolosi, Graphene and MXene-based transparent conductive electrodes and supercapacitors. *Energy Storage Mater*. **16**, 102–125 (2019).
40. G. Ying, S. Kota, A. D. Dillon, A. T. Fafarman, M. W. Barsoum, Conductive transparent V_2CT_x (MXene) films. *FlatChem*. **8**, 25–30 (2018).
41. P. Salles, E. Quain, N. Kurra, A. Sarycheva, Y. Gogotsi, Automated Scalpel Patterning of Solution Processed Thin Films for Fabrication of Transparent MXene Microsupercapacitors. *Small*. **14**, 1802864 (2018).
42. A. Ghicov, H. Tsuchiya, R. Hahn, J. M. Macak, A. G. Muñoz, P. Schmuki, TiO_2 nanotubes: H^+ insertion and strong electrochromic effects. *Electrochem. Commun.* **8**, 528–532 (2006).
43. J. Z. Chen, W. Y. Ko, Y. C. Yen, P. H. Chen, K. J. Lin, Hydrothermally Processed TiO_2 Nanowire Electrodes with Antireflective and Electrochromic Properties. *ACS Nano*. **6**, 6633–6639 (2012).
44. N. N. Dinh, N. Th. T. Oanh, P. D. Long, M. C. Bernard, A. H. Goff, Electrochromic properties of TiO_2 anatase thin films prepared by a dipping sol-gel method. *Thin Solid Films*. **423**, 70–76 (2003).
45. Z. Tebby, O. Babot, T. Toupance, D. H. Park, G. Campet, M. H. Delville, Low-Temperature UV-Processing of Nanocrystalline Nanoporous Thin TiO_2 Films: An Original Route toward Plastic Electrochromic Systems. *Chem. Mater.* **20**, 7260–7267 (2008).
46. Y. Chen, X. Li, Z. Bi, X. He, G. Li, X. Xu, X. Gao, Design and construction of hierarchical TiO_2 nanorod arrays by combining layer-by-layer and hydrothermal crystallization techniques for electrochromic application. *Appl. Surf. Sci.* **440**, 217–223 (2018).
47. R. A. Patil, R. S. Devan, Y. Liou, Y. R. Ma, Efficient electrochromic smart windows of one-dimensional pure brookite TiO_2 nanoneedles. *Sol. Energy Mater. Sol. Cells*. **147**, 240–245 (2016).
48. Y. Chen, X. Li, Z. Bi, X. He, X. Xu, X. Gao, Core-Shell Nanorod Arrays of Crystalline/Amorphous TiO_2 Constructed by Layer-by-Layer Method for High-Performance Electrochromic Electrodes. *Electrochim. Acta*. **251**, 546–553 (2017).
49. Y. Alesanco, J. Palenzuela, R. Tena-Zaera, G. Cabañero, H. Grande, B. Herbig, A. Schmitt, M. Schott, U. Posset, A. Guerfi, M. Dontigny, K. Zaghib, A. Viñuales, Plastic electrochromic devices based on viologen-modified TiO_2 films prepared at low temperature. *Sol. Energy Mater. Sol. Cells*. **157**, 624–635 (2016).
50. R. Li, K. Li, G. Wang, L. Li, Q. Zhang, J. Yan, Y. Chen, Q. Zhang, C. Hou, Y. Li, H. Wang, Ion-Transport Design for High-Performance Na^+-Based Electrochromics. *ACS Nano*. **12**,

3759–3768 (2018).
51. J. L. Wang, Y. R. Lu, H. H. Li, J. W. Liu, S. H. Yu, Large Area Co-Assembly of Nanowires for Flexible Transparent Smart Windows. *J. Am. Chem. Soc.* **139**, 9921–9926 (2017).
52. Q. Zhang, C. Y. Tsai, L. J. Li, D. J. Liaw, Colorless-to-colorful switching electrochromic polyimides with very high contrast ratio. *Nat. Commun.* **10**, 1239 (2019).
53. E. Hwang, S. Seo, S. Bak, H. Lee, M. Min, H. Lee, An Electrolyte-Free Flexible Electrochromic Device Using Electrostatically Strong Graphene Quantum Dot–Viologen Nanocomposites. *Adv. Mater.* **26**, 5129–5136 (2014).
54. S. Cao, S. Zhang, T. Zhang, J. Y. Lee, Fluoride-Assisted Synthesis of Plasmonic Colloidal Ta-Doped TiO_2 Nanocrystals for Near-Infrared and Visible-Light Selective Electrochromic Modulation. *Chem. Mater.* **30**, 4838–4846 (2018).
55. S. H. Lee, H. M. Cheong, C. E. Tracy, A. Mascarenhas, A. W. Czanderna, S. K. Deb, Electrochromic coloration efficiency of a-WO_3-y thin films as a function of oxygen deficiency. *Appl. Phys. Lett.* **75**, 1541–1543 (1999).
56. X. H. Rui, N. Ding, J. Liu, C. Li, C. H. Chen, Analysis of the chemical diffusion coefficient of lithium ions in $Li_3V_2(PO_4)_3$ cathode material. *Electrochim. Acta*. **55**, 2384–2390 (2010).
57. E. Pehlivan, G. A. Niklasson, C. G. Granqvist, P. Georén, Ageing of electrochromic WO_3 coatings characterized by electrochemical impedance spectroscopy. *Phys. Status Solidi A*. **207**, 1772–1776 (2010).
58. S. B. Tang, M. O. Lai, L. Lu, Study on Li^+-ion diffusion in nano-crystalline $LiMn_2O_4$ thin film cathode grown by pulsed laser deposition using CV, EIS and PITT techniques. *Mater. Chem. Phys*. **111**, 149–153 (2008).

Acknowledgments

Author contributions: R. L. and X. M. performed most of experiments. R. L., X. M., X. Z. and L. W. prepared the samples, J. L., J. C., H. G. and T. L. characterized the samples. G. W., C. H. and Y. L. analyzed the data, Q. Z., R. L., Y. L., Y. L., H. W. and X. L. designed experiments. All authors discussed the results and commented on the manuscript.

Funding: X. L., J. C., T. L. and T. P. acknowledge the support from Semiconductor Research Corporation (SRC). X. L. acknowledge the membership of the Photonics Centers at Boston University. H. W. and R. L. acknowledge the financial support of the Natural Science Foundation of China (Grant No.51972054), Fundamental Research Funds for the Central Universities (18D110308). R. L. acknowledge the support of Graduate Student Innovation Fund of Donghua University (CUSF-DH-D-2019002).

Competing interests: The authors declare that they have no competing interests.

Data and materials availability: All data needed to evaluate the conclusions in the paper are present in the paper and/or the Supplementary Materials. Additional data related to this paper may be requested from the authors.

Figures and Tables

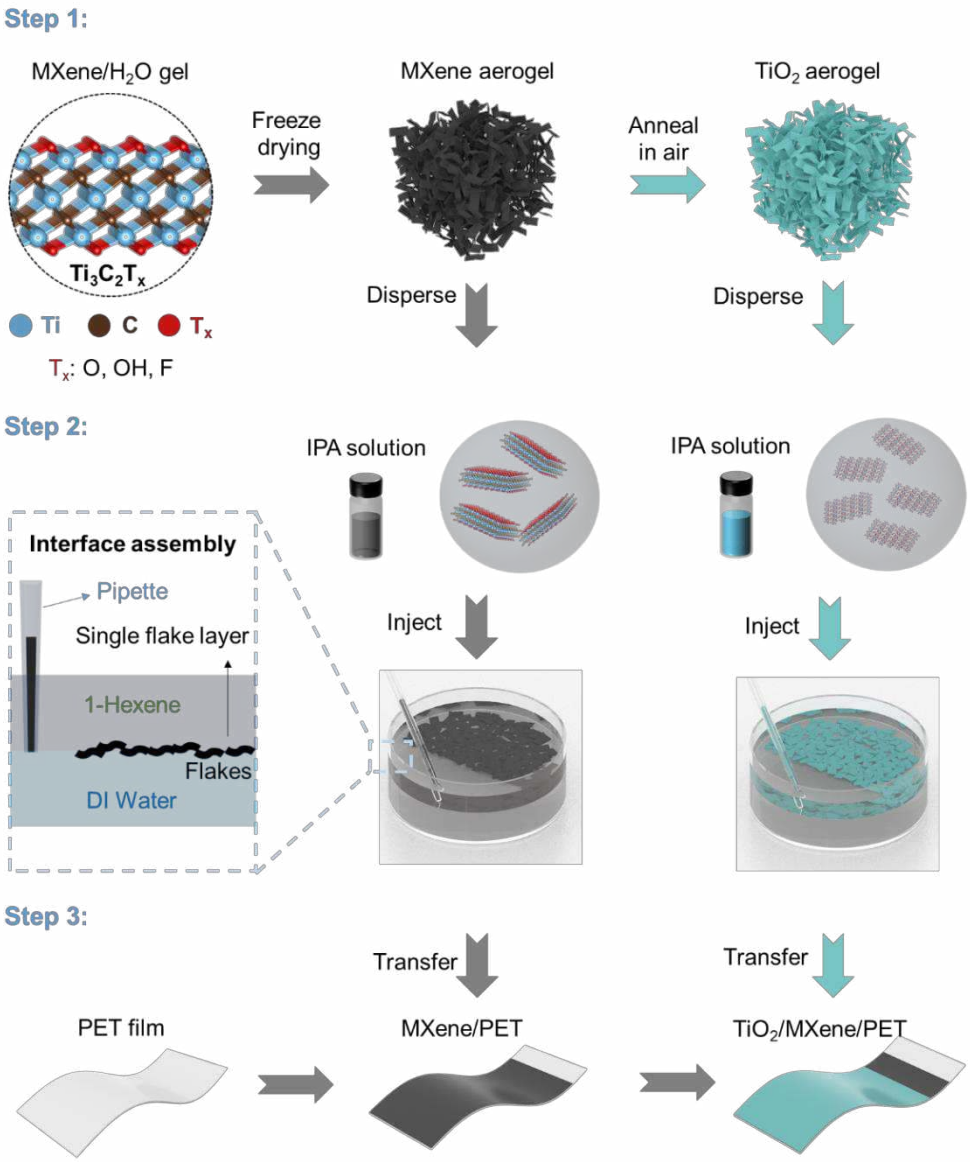

Fig. 1. Fabrication process of $TiO_2/Ti_3C_2T_x$ heterostructure on a flexible substrate. Step 1: MXene ($Ti_3C_2T_x$) aerogel is obtained by freeze drying of the $Ti_3C_2T_x$ nanosheets dispersion and the derived TiO_2 aerogel is obtained by annealing the MXene aerogel in air at 400°C. Step 2: $Ti_3C_2T_x$ and TiO_2 2D nanosheets are dispersed respectively in IPA, injected into the interface between hexene and DI water, and self-assembled into nanometer-thick $Ti_3C_2T_x$ and TiO_2 films. Step 3: the thin films are transferred onto a flexible substrate (e.g. PET) in a layer-by-layer fashion to realize the TiO_2/MXene heterostructure, where the TiO_2 layer serves as the electrochromic component, and the MXene layer serves as the transparent electrode.

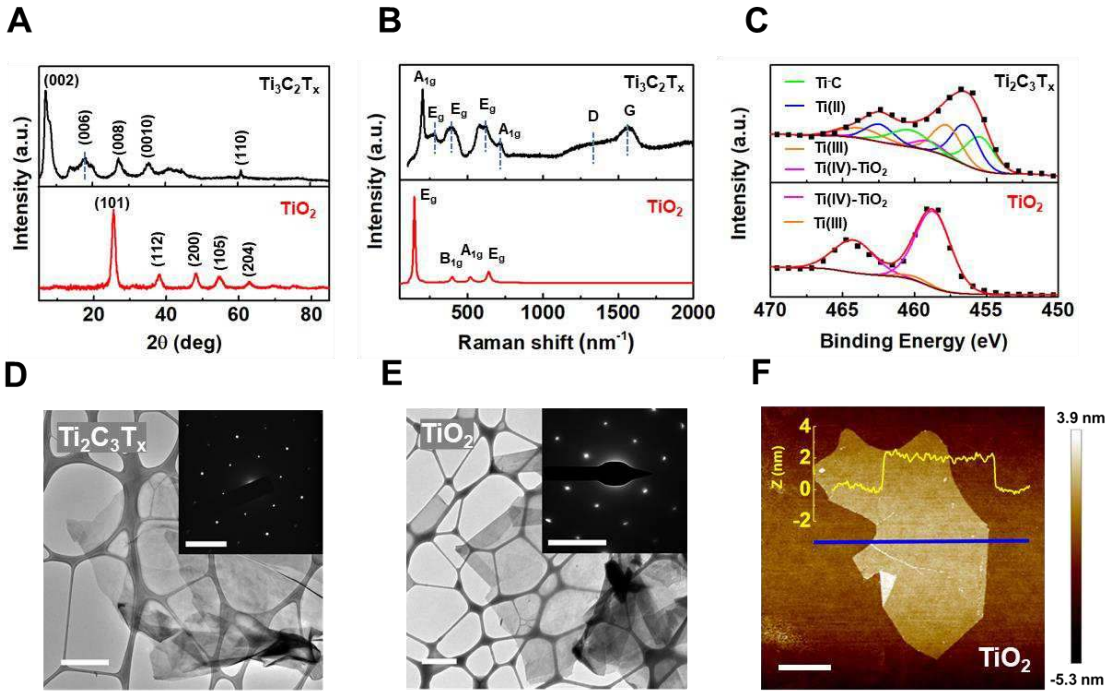

Fig. 2. Conversion of $Ti_3C_2T_x$ into 2D TiO_2 flakes. (A) XRD patterns and (B) Raman spectra of the $Ti_3C_2T_x$ before and after annealing at 400°C for 50 h. (C) XPS spectra of the $Ti_3C_2T_x$ and the derived TiO_2. TEM images of (E) $Ti_3C_2T_x$ and (F) derived TiO_2 flakes on a TEM grid (scale bar: 1 μm). Insets: SEAD patterns of $Ti_3C_2T_x$ and derived TiO_2 flakes (scale bar: 5 nm^{-1}); (F) AFM image and height profile of a derived TiO_2 flake on a SiO_2/Si substrate (scale bar: 2 μm).

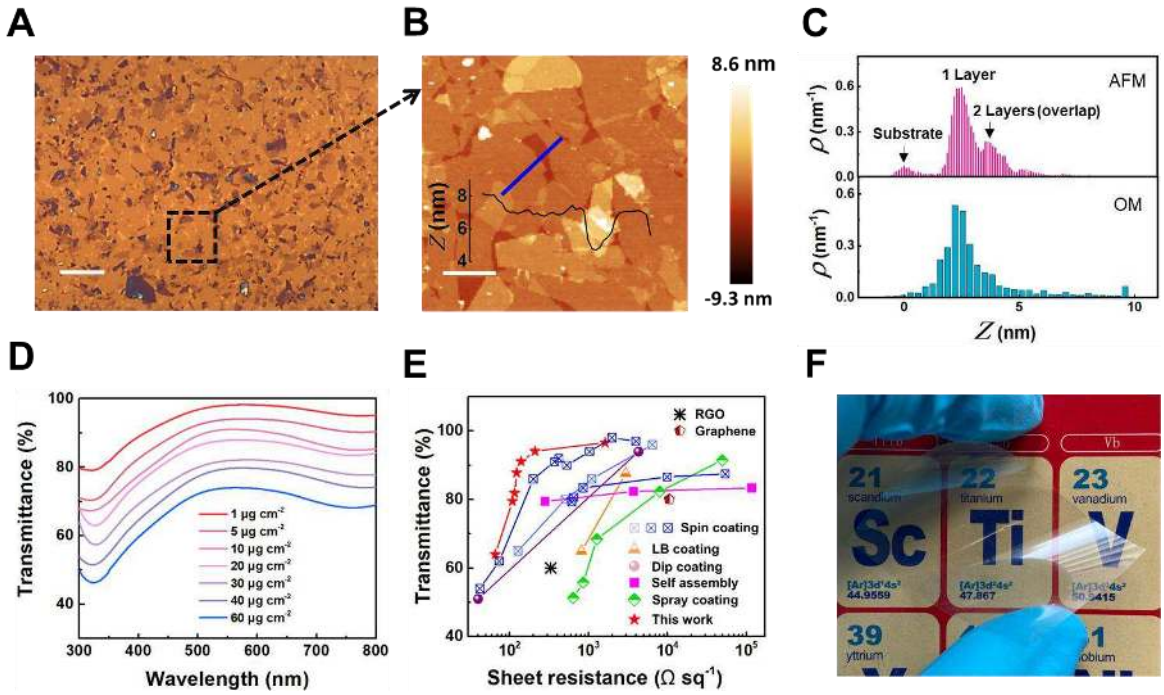

Fig. 3. Characterization of the self-assembled $Ti_3C_2T_x$ thin film as a transparent electrode. (A) OM image of the assembled $Ti_3C_2T_x$ thin film (scale bar: 10 μm). (B) AFM image and the height profile of the assembled $Ti_3C_2T_x$ thin film in corresponding area marked in (A) (scale bar: 2 μm). (C) Height distributions extracted from the AFM image (top) and the OM image (bottom); the y-axes are probability density, namely, frequency per unit height; (D) Transmittance spectra of $Ti_3C_2T_x$ films with various concentrations of injected $Ti_3C_2T_x$; (E) Transmittance at 550 nm as a function of sheet resistance for the $Ti_3C_2T_x$ films and data from previously reported transparent electrode technologies; (F) Photograph of a Ti_3C_2Tx film deposited on a PET substrate that presents excellent transparency and flexibility.

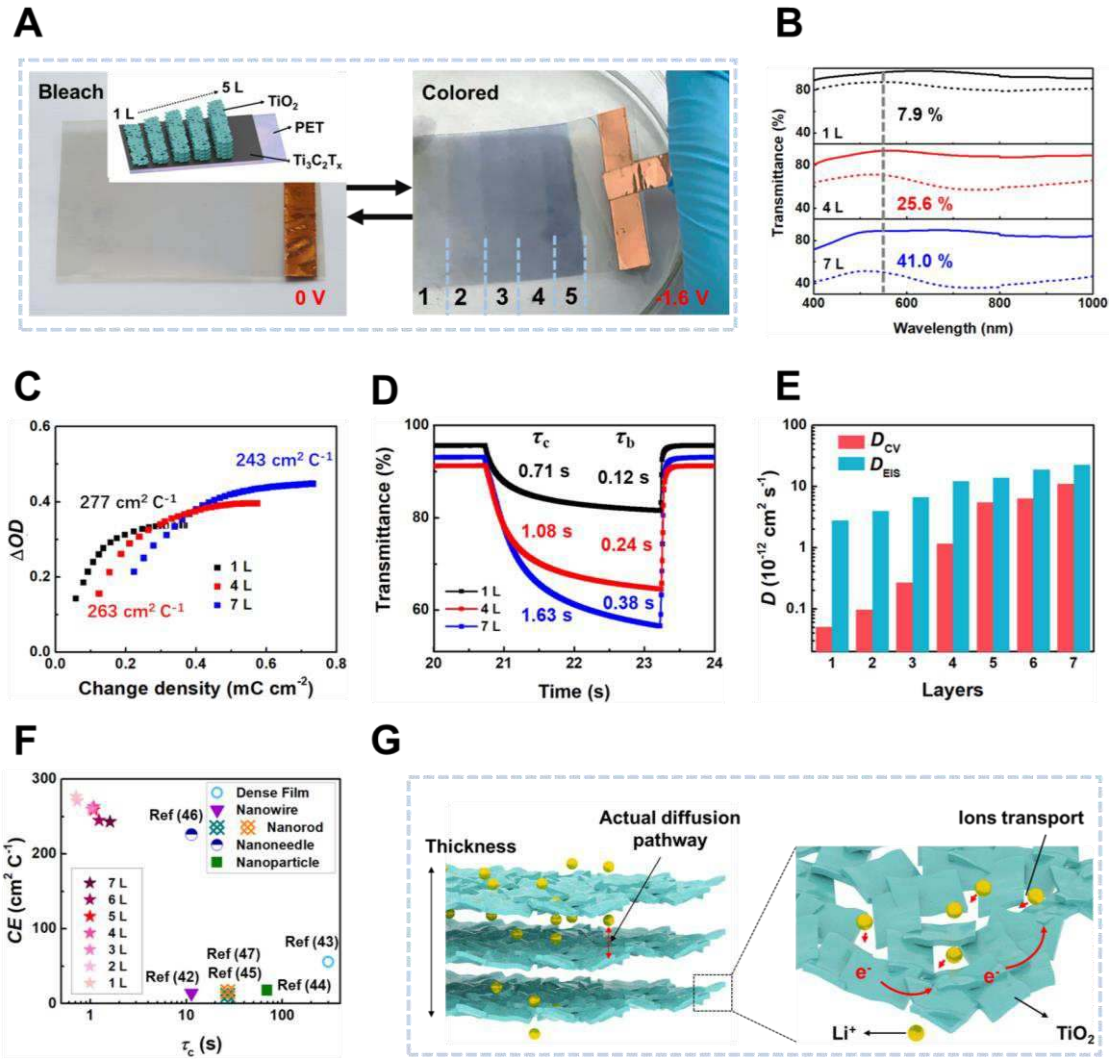

Fig. 4. Electrochromic properties of the $TiO_2/Ti_3C_2T_x$ heterostructure. (A) Photographs of the $TiO_2/Ti_3C_2T_x$/PET film with different layers of TiO_2 at the bleach state (no bias) and the colored state (biased at -1.6 V). Inset: structure of $TiO_2/Ti_3C_2T_x$/PET film with different TiO_2 layers; (B) Optical transmittance spectra with 1, 4 and 7 layers of TiO_2 at the biases of 0 V (solid) and -1.6 V (dotted). (C) Optical density change (ΔOD) as a function of the injected charge density for the heterostructures with 1, 4 and 7 layers of TiO_2; (D) Temporal response of the transmittance at 550 nm of the heterostructures with 1, 4 and 7 layers of TiO_2. (E) Diffusion coefficients (D) of the heterostructures with 1–7 layers of TiO_2 extracted from the EIS and CV measurements; (F) CE as a function of coloration time (τ_c) for the $TiO_2/Ti_3C_2T_x$ heterostructures and previously reported TiO_2-based structures; (G) Schematic of the pathways of electron conduction and ion diffusion within the self-assembled TiO_2 thin film.

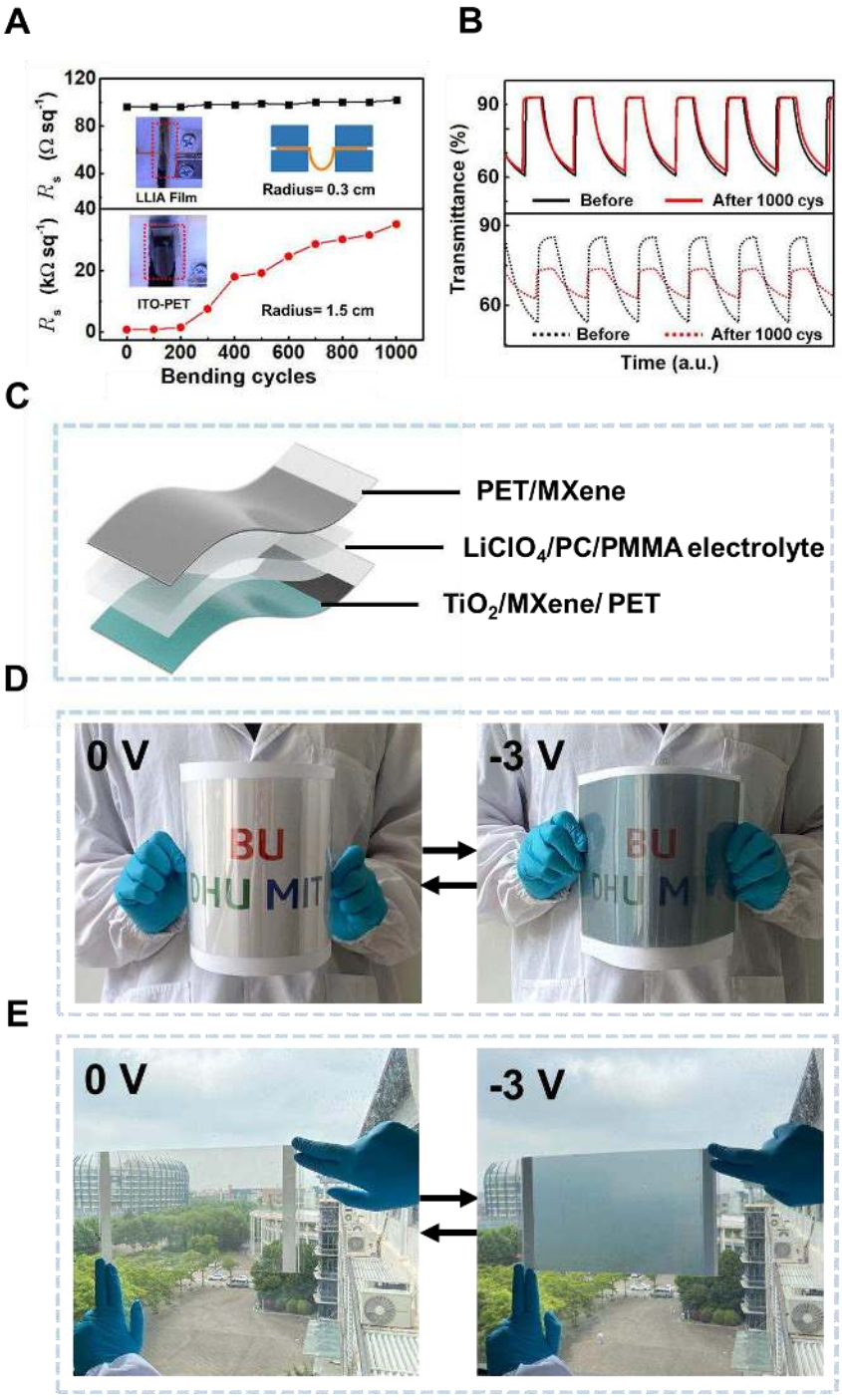

Fig. 5. Mechanical properties of the $TiO_2/Ti_3C_2T_x$ heterostructure and demonstration of a large-area flexible EC device. (A) Comparison of the sheet resistance (R_s) of the LLIA $Ti_3C_2T_x$/PET and the ITO/PET films after 1000 bending cycles. (B) Comparison of the electrochromic switching behaviors of the LLIA $TiO_2/Ti_3C_2T_x$/PET and the ITO/PET films after 1000 bending cycles. (C) Schematic diagram of the flexible solid electrochromic device; (D, E) Photographs of the as-prepared solid electrochromic device with an A4 paper size (about 20 cm×30 cm).

Figures

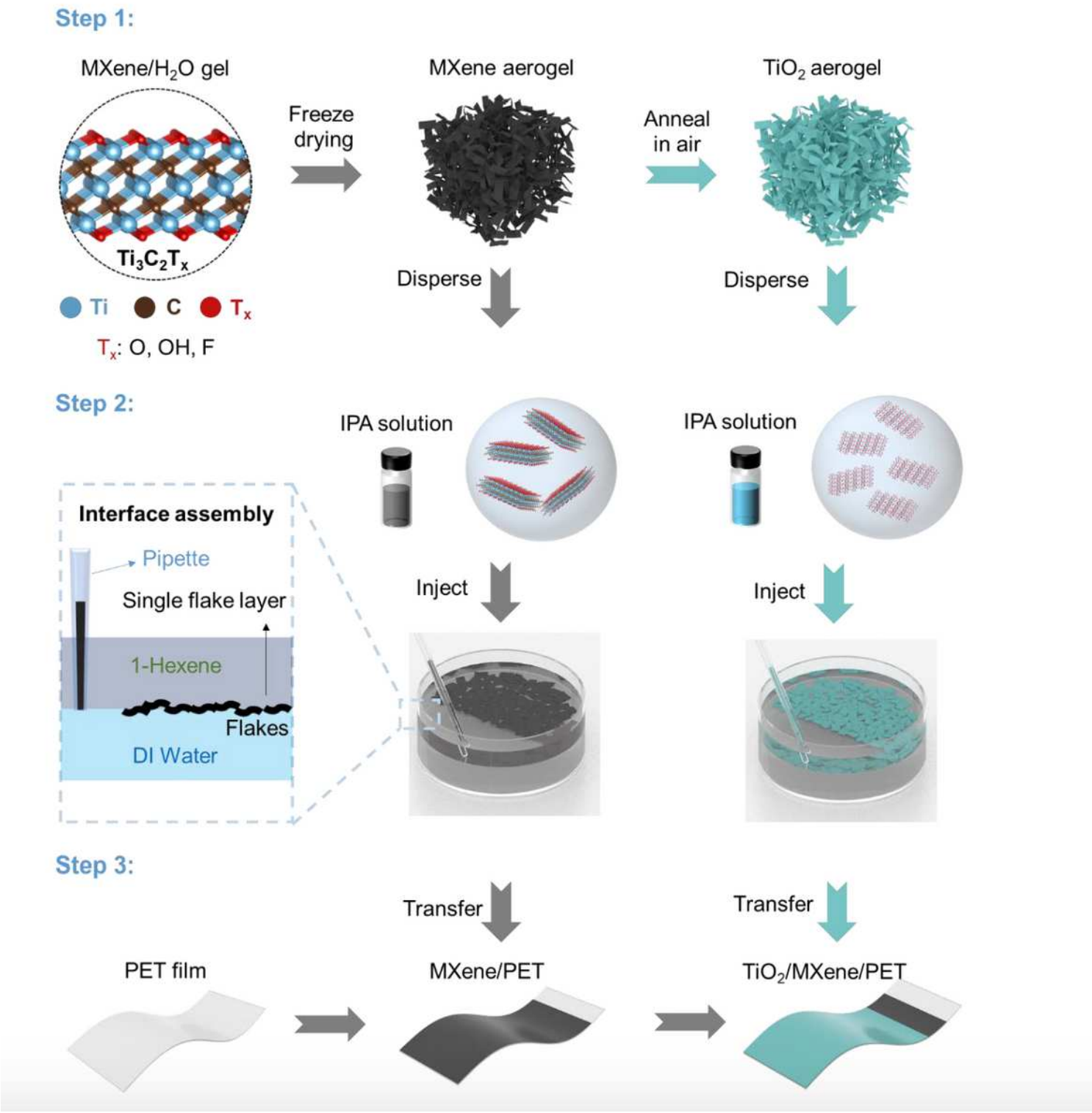

Figure 1

Fabrication process of TiO2/Ti3C2Tx heterostructure on a flexible substrate. Step 1: MXene (Ti3C2Tx) aerogel is obtained by freeze drying of the Ti3C2Tx nanosheets dispersion and the derived TiO2 aerogel is obtained by annealing the MXene aerogel in air at 400°C. Step 2: Ti3C2Tx and TiO2 2D nanosheets are

dispersed respectively in IPA, injected into the interface between hexene and DI water, and self-assembled into nanometer-thick Ti3C2Tx and TiO2 films. Step 3: the thin films are transferred onto a flexible substrate (e.g. PET) in a layer-by-layer fashion to realize the TiO2/MXene heterostructure, where the TiO2 layer serves as the electrochromic component, and the MXene layer serves as the transparent electrode.

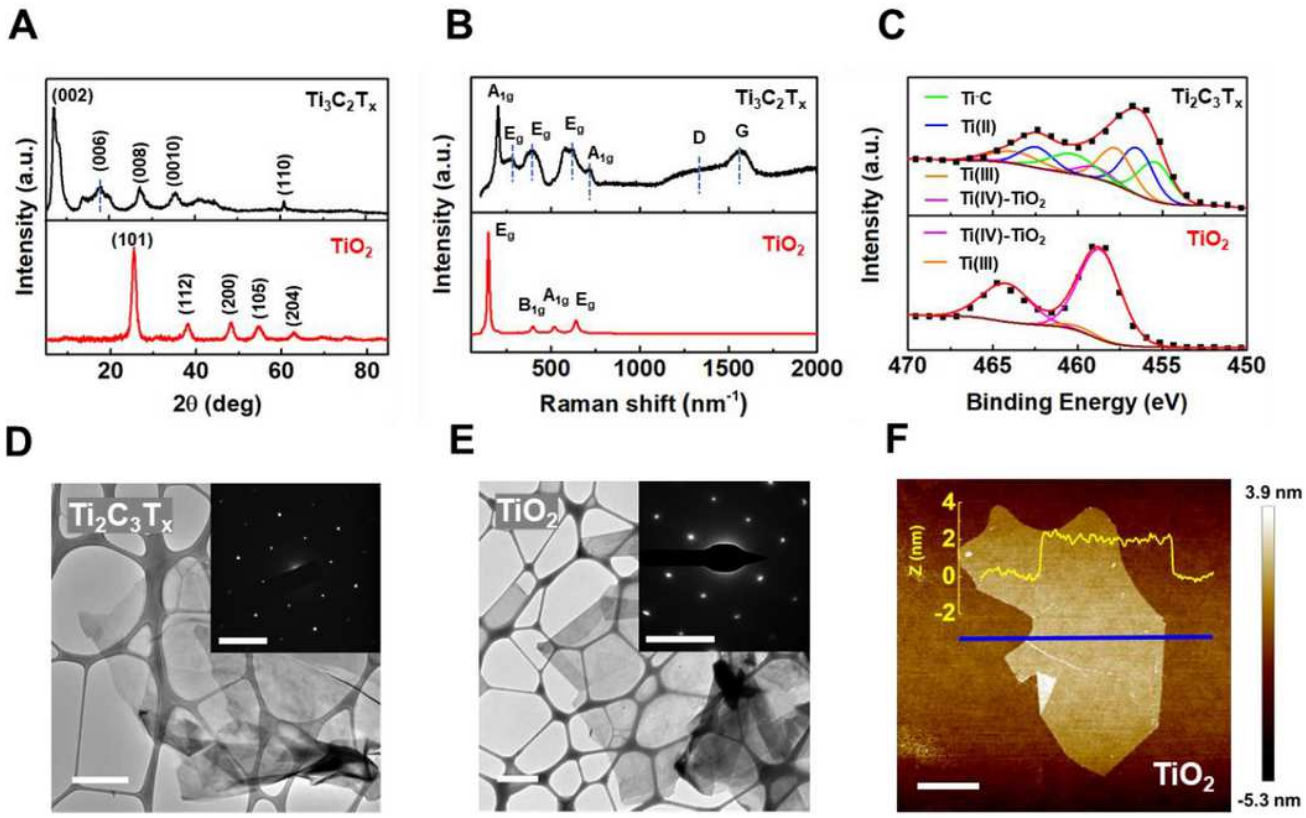

Figure 2

Conversion of Ti3C2Tx into 2D TiO2 flakes. (A) XRD patterns and (B) Raman spectra of the Ti3C2Tx before and after annealing at 400°C for 50 h. (C) XPS spectra of the Ti3C2Tx and the derived TiO2. TEM images of (E) Ti3C2Tx and (F) derived TiO2 flakes on a TEM grid (scale bar: 1 μm). Insets: SEAD patterns of Ti3C2Tx and derived TiO2 flakes (scale bar: 5 nm-1); (F) AFM image and height profile of a derived TiO2 flake on a SiO2/Si substrate (scale bar: 2 μm).

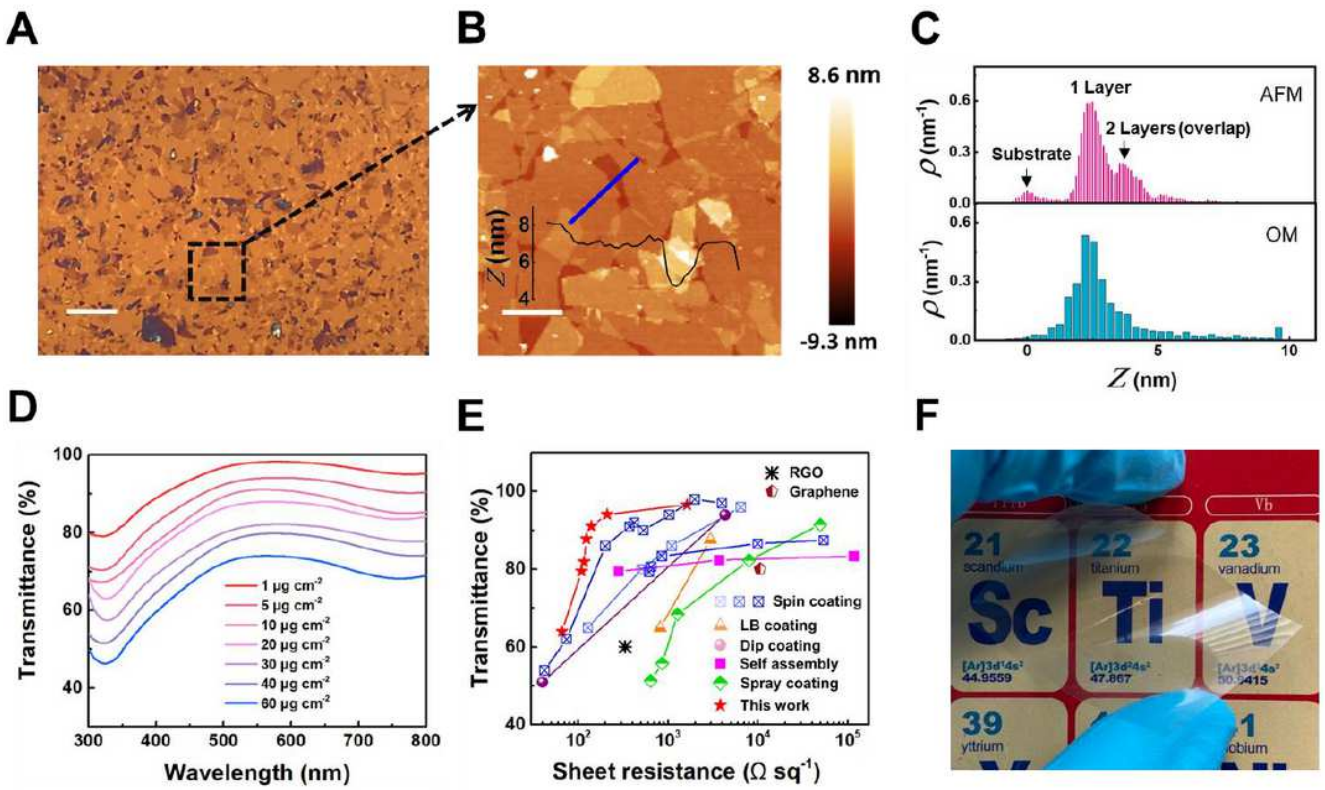

Figure 3

Characterization of the self-assembled Ti3C2Tx thin film as a transparent electrode. (A) OM image of the assembled Ti3C2Tx thin film (scale bar: 10 μm). (B) AFM image and the height profile of the assembled Ti3C2Tx thin film in corresponding area marked in (A) (scale bar: 2 μm). (C) Height distributions extracted from the AFM image (top) and the OM image (bottom); the y-axes are probability density, namely, frequency per unit height; (D) Transmittance spectra of Ti3C2Tx films with various concentrations of injected Ti3C2Tx; (E) Transmittance at 550 nm as a function of sheet resistance for the Ti3C2Tx films and data from previously reported transparent electrode technologies; (F) Photograph of a Ti3C2Tx film deposited on a PET substrate that presents excellent transparency and flexibility.

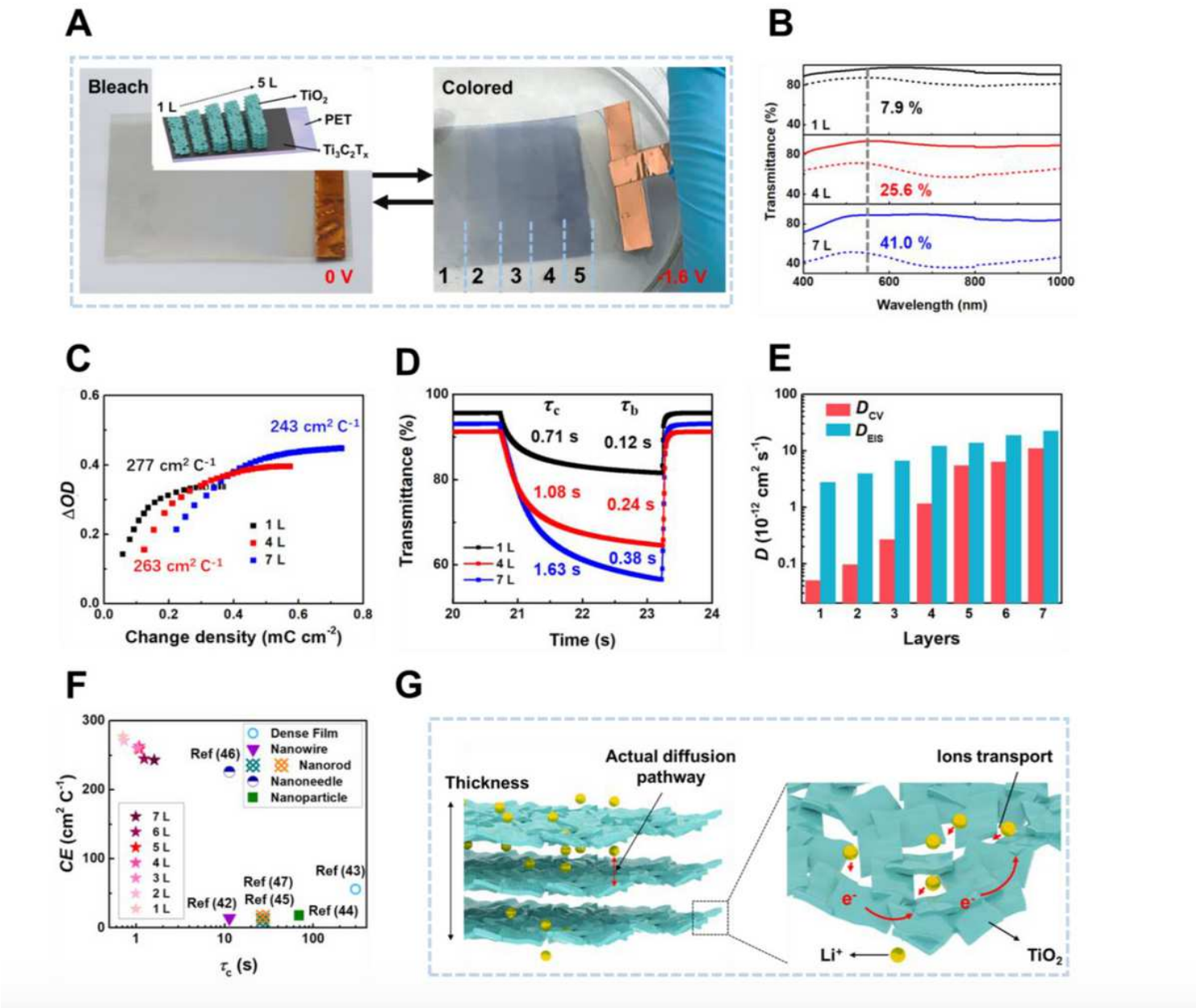

Figure 4

Electrochromic properties of the TiO2/Ti3C2Tx heterostructure. (A) Photographs of the TiO2/Ti3C2Tx/PET film with different layers of TiO2 at the bleach state (no bias) and the colored state (biased at -1.6 V). Inset: structure of TiO2/Ti3C2Tx/PET film with different TiO2 layers; (B) Optical transmittance spectra with 1, 4 and 7 layers of TiO2 at the biases of 0 V (solid) and -1.6 V (dotted). (C) Optical density change (ΔOD) as a function of the injected charge density for the heterostructures with 1, 4 and 7 layers of TiO2; (D) Temporal response of the transmittance at 550 nm of the heterostructures with 1, 4 and 7 layers of TiO2. (E) Diffusion coefficients (D) of the heterostructures with 1–7 layers of TiO2 extracted from the EIS and CV measurements; (F) CE as a function of coloration time (τc) for the TiO2/Ti3C2Tx heterostructures and previously reported TiO2-based structures; (G) Schematic of the pathways of electron conduction and ion diffusion within the self-assembled TiO2 thin film.

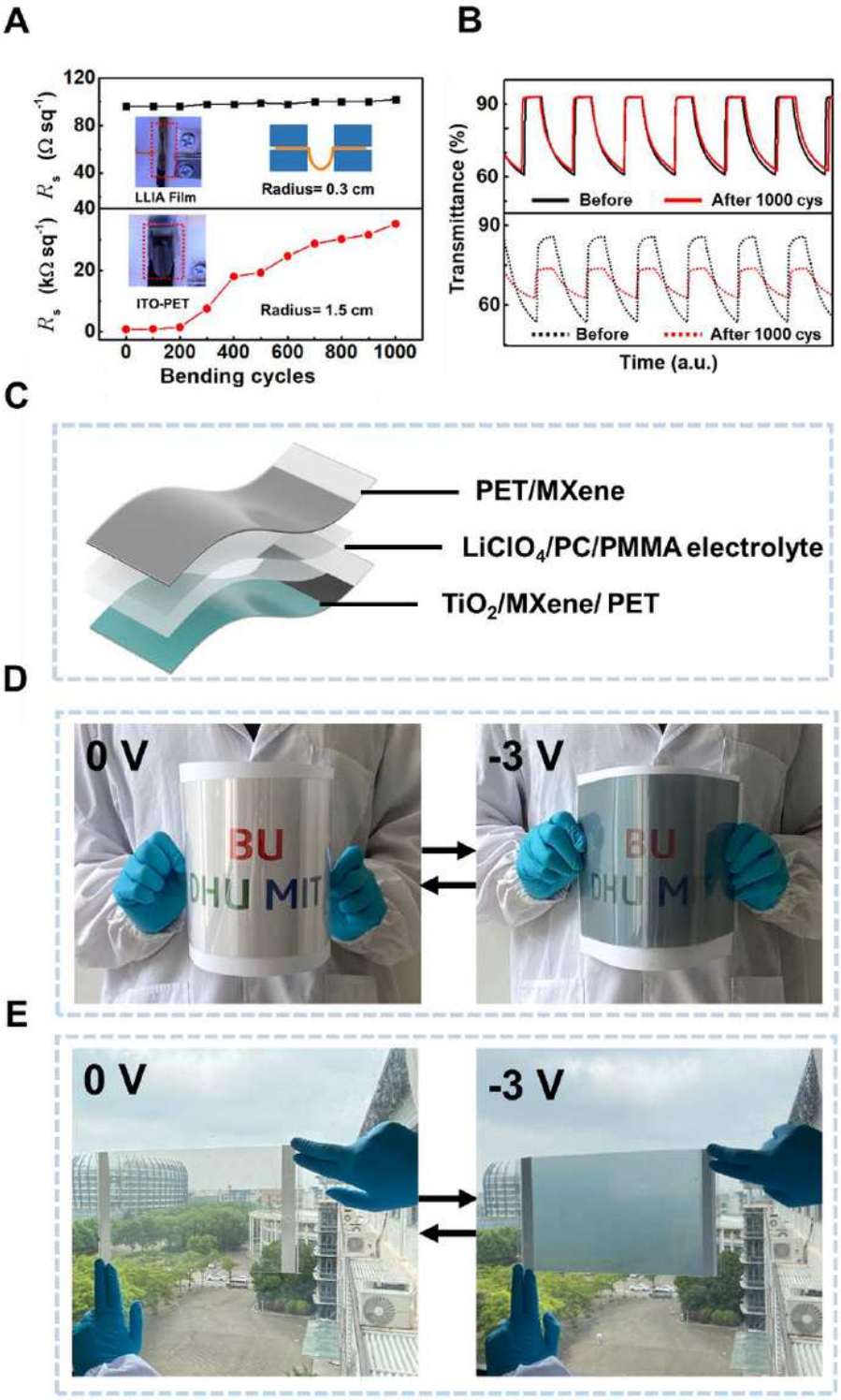

Figure 5

Mechanical properties of the TiO2/Ti3C2Tx heterostructure and demonstration of a large-area flexible EC device. (A) Comparison of the sheet resistance (Rs) of the LLIA Ti3C2Tx/PET and the ITO/PET films after 1000 bending cycles. (B) Comparison of the electrochromic switching behaviors of the LLIA TiO2/Ti3C2Tx/PET and the ITO/PET films after 1000 bending cycles. (C) Schematic diagram of the

flexible solid electrochromic device; (D, E) Photographs of the as-prepared solid electrochromic device with an A4 paper size (about 20 cm×30 cm).

Supplementary Files

This is a list of supplementary files associated with this preprint. Click to download.

- SI.pdf